Simulating spatial and temporal evolution of multiple wing cracks around faults in crystalline basement rocks

Jonathan P. Willson[1], Rebecca J. Lunn[2], Zoe K. Shipton[3]*

[1]School of the Built Environment, Heriot-Watt University, Edinburgh, Scotland

[2]Department of Civil Engineering, University of Strathclyde, Glasgow, Scotland

[3]Department of Geographical and Earth Sciences, University of Glasgow, Scotland

Running title: Wing crack evolution around faults

Keywords: mechanical modeling, faults, splay fractures, damage zone, dynamic

Abstract

Faults zones are structurally highly spatially heterogeneous and hence extremely complex. Observations of fluid flow through fault zones over several scales show that this structural complexity is reflected in the hydrogeological properties of faults. Information on faults at depth is scarce, hence, it is highly valuable to understand the controls on spatial and temporal fault zone development. In this paper we increase our understanding of fault damage zone development in crystalline rocks by dynamically simulating the growth of single and multiple splay fractures produced from failure on a pre-existing fault. We present a new simulation model, MOPEDZ, that simulates fault evolution through solution of Navier's equation with a combined Mohr-Coulomb and tensile failure criteria. Simulations suggest that location, frequency, mode of failure and orientation of splay fractures are significantly affected both by the orientation of the fault with respect to the maximum principal compressive stress and the conditions of differential stress. Model predictions compare well with published field outcrop data, confirming that this model produces realistic damage zone geometries.

Introduction

Faults are structurally highly spatially heterogeneous and hence extremely complex [*Aydin*, 2000; *Caine et al.*, 1996; *do Nascimento et al.*, 2005; *Fairley and Hinds*, 2004; *Galli et al.*, 2004; *Wibberley and Shimamoto*, 2003]. Observations of spatially heterogeneous fluid flow through fault zones over several scales e.g. [*do Nascimento et al.*, 2005; *Fairley and Hinds*, 2004] show that this structural complexity is reflected in the hydrogeological properties of faults. Within crystalline basement rocks, permeable faults are a dominant feature of subsurface flow systems. The dominant deformation structures in these systems are fractures that may be open or filled with minerals or gouge. Recent research at the European Union's Soultz-sous-Forêt Hot Dr y Rock test site [*Evans et al.*, 2005a], underlines the importance of characterising fault zones. Data taken from low pressure injection tests on the open borehole at Soultz show that almost all flow occurs within a single fault zone located at 3490 m depth, and that just 10 major open fractures account for 95% of the flow.

Fault zone structure can also vary temporally due to continued movement on the fault and/or changing stress conditions. This can result in the creation of new fractures and the reopening of sealed existing fractures, both of which may lead to increased fault zone permeability. Observations during the high pressure injection tests at the HDR Soultz-sous-Forêt site confirm this link between fault damage zone evolution and increased flow to the borehole [*Evans*, 2005; *Evans et al.*, 2005b; *Evans et al.*, 2005c]). Temporal changes in fault hydraulic properties have also been observed in the hydrocarbon industry [*Anderson et al.*, 1994; *Losh*, 1998; *Losh*, 2006].

The inaccessibility of subsurface faults, in combination with their spatial and temporal complexity, makes it hard either to assess fault architectural structure or to predict fault permeability. Data from boreholes and seismic surveys are available, however neither provide the information necessary to constrain values of fault permeability. Given the scarcity of information on faults at depth, it is advantageous to gain as much knowledge as possible on the processes that govern spatial and temporal fault zone development. Ultimately, if these processes can be numerically simulated, then predicted fault zone architectures can be up-scaled to provide statistical estimates of bulk permeability fields. The aim of our research is to predict damage zone features on small (subseismic) faults with geometries that are geologically realistic. It is particularly important for estimation of bulk fault permeability in crystalline rocks to accurately simulate the orientation and connected nature of evolving fractures. In this paper, we present the first stage in achieving this aim; simulating the dynamic growth of single and multiple splay fractures produced from failure on pre-existing faults or joints.

Previous simulation studies of fault damage zone development

A number of researchers have employed numerical simulation methods to predict the evolution of damage zone features surrounding faults. The modeling studies of [*Burgmann et al.*, 1994; *Du and Aydin*, 1993; 1995] employ Linear Elastic Fracture Mechanics, first presented in [*Pollard and Segall*, 1987], to simulate the growth of splay fractures from original faults or joints. [*Du and Aydin*, 1995] calculate the distribution of strain energy around pre-existing features such as isolated fault tips, echelon fault steps

and fault bends, and infer the directions of propagating fractures from the direction of maximum distortional strain energy. [*Shen and Stephansson*, 1993] simulate the propagation of shear fractures using the F-criteria based on combining the Maximum Principal Stress and the Maximum Strain Energy Release Rate criteria, which they propose for simulation of Mode I and Mode II fractures. Using the F-criteria, they simulate damage at the fault tips whereby an initial single high angle tension fracture evolves followed by a single shear fracture that propagates in the same direction as the original fault.

More recently, research has focused on simulation of fault zone damage from dynamic fault rupture in seismically active faults to improve estimates of energy losses during earthquakes. [*Yamashita*, 2000] combines laboratory experiments with numerical simulation to predict the generation of microcracks during macroscopic shear rupture. He simulates the temporal evolution of maximum tensile stress at a rupture tip to infer the location and orientation of associated microcracks in the surrounding rock. He concludes that dynamically propagating earthquake faults generate a large number of tensile microcracks in the surrounding fault zone. [*Dalguer et al.*, 2003] develop and apply a 3D Discrete Element Model to simulate crack propagation during the seismic rupture of a pre-existing fault. They simulate the generation of new cracks within the surrounding fault zone caused by progression of a single rupture patch on the fault with a tensile failure criterion: as the rupture front progresses, tensile cracks expand and new cracks are generated at the tip of the dynamic rupture patch.

In this paper we extend fault zone modeling of fault growth, such as that by [*Burgmann et al.*, 1994; *Du and Aydin*, 1993; 1995; *Shen and Stephansson*, 1993], to include spatial and temporal evolution of single and multiple wing cracks within a fault damage zone in crystalline basement. The model presented here introduces several novel processes that have not been previously accounted for: cracks are propagated dynamically based on the temporally evolving stress field; simulations investigate progressive microscopic-to-macroscopic failure; the model uses a combined Mohr Coulomb and tensile failure criterion that allows for both shear and tensile failure of the rock.

Formulation of a Numerical Model for the Evolution of Fault Damage Zones

This paper presents a new model for the simulation of fault damage zone evolution. The code is a two-dimensional coupled hydro-mechanical model, MOPEDZ (Modelling Of Permeability Evolution in the Damage Zone surrounding faults), and is based on a finite element approach to solving Navier's equation with a combined Mohr Coulomb-tensile failure criterion, coupled to the groundwater flow equation [*Willson et al.*, 2005]. We present the results of simulations using the mechanical modeling component of MOPEDZ in order to investigate the controls on the evolution of wing crack generation around a single pre-existing fault.

Navier's equation is well known as describing the displacement of a body subject to external forcing. The steady-state form of the equation can be written as

$$\nabla \cdot c\nabla \mathbf{u} = \mathbf{F} \qquad (1)$$

Where **F** is the vector of external forces, **u** is a vector describing displacement and *c* is a matrix where each entry is a function of the first and second Lamé constants. The failure criteria employed to simulate rock fracturing in MOPEDZ are the Mohr-Coulomb and tensile failure criteria, generally written as

$$\sigma_1 \le C_0 + \left[\left(\mu^2 + 1\right)^{1/2} + \mu\right]^2 \sigma_3 \text{ and } \sigma_3 \le -T_0 \qquad (2)$$

respectively, where σ_1 is the maximum principal compressive stress, σ_3 is the minimum principal compressive stress, C_0 is the uniaxial compressive strength, μ is the coefficient of friction and T_0 is the tensile strength.

MOPEDZ is built using the commercially available finite element software, FEMLAB [COMSOL, 2004]. FEMLAB is used to provide finite element subroutines that are called from the MOPEDZ code, which has been developed, and is executed, within MATLAB. MOPEDZ models the propagation of fractures by solution of Navier's equation. Failure is predicted by a combined Mohr-Coulomb and tensile failure criterion, which results in changes to the material parameters at failed locations. Elements that contain fractures (as opposed to intact host rock only) are represented by a reduction in the values of Young's Modulus, Poisson's ratio and the material strength. This approach is similar to that of [*Tang*, 1997] which has been successfully applied to simulate laboratory experiments and reproduce fracture patterns around tunnels and boreholes.

The aim of MOPEDZ is to reproduce the change in material properties (Young's Modulus, Poisson's ratio and the material strength) of a rock as it fails i.e. the first failure is triggered by a deformation of the boundaries, but subsequent failures can occur

143 spontaneously because of stress redistribution around previous failures. These subsequent
144 failures can be adjacent to previous failures, i.e. the extension of a fracture, or they can
145 occur in locations that are disconnected from any previous failure, but fail because of the
146 redistribution of stress. MOPEDZ solves Navier's equation as a progressive series of
147 steady-states. Initially, the top and bottom boundaries of the model domain are displaced
148 inwards by a small increment. Navier's equation is then solved and the number of
149 predicted failures examined. The displacement increment is then adjusted, and Navier's
150 equation re-solved, such that a pre-defined small number of elements are predicted to fail,
151 resulting in a reduction in material properties for those elements. This approach of
152 numerically representing fracturing of an element of rock by reducing its material
153 properties was first developed and validated in rock mechanics using laboratory data
154 [*Tang*, 1997]. After the material properties have been reduced within MOPEDZ, Navier's
155 equation is resolved (with no further boundary displacement). If elements are still
156 predicted to fail, the same process is repeated until no more failure is predicted i.e. a
157 steady-state is reached. Once a steady-state solution has been achieved for a given
158 boundary displacement, the boundaries are once more displaced to produce further shear
159 damage and the whole solution process is repeated.
160
161 The restriction of only a few elements for failure within each iterative solution ensures
162 stability of the model solution and a temporal propagation of cracks upon failure. For all
163 the simulations presented here, the number of failures for a single boundary displacement
164 was 10. In general, the higher the displacement, the more rapidly the model runs. Ten

165 failures were selected as it produced results almost identical to those allowing only a
166 single failure with each iteration.
167
168 **Results**
169 Figure 1 shows the temporal evolution of damage for a pre-existing fault with an
170 orientation of 30˚ to the maximum principal stress. In all simulations presented in this
171 paper, the maximum principal stress is orientated along the y-axis (i.e. top-to-bottom).
172 The accompanying simulation parameters (Table 1) are based on available laboratory
173 data for granite. In this simulation, σ_3=0 on the lateral boundaries of the model and the
174 top and bottom boundaries are gradually displaced inwards as described above. Note that
175 the position of the pre-existing fault is non-central, with the fault being located slightly to
176 the right hand side of the domain. Figure 1 shows progressive temporal development of a
177 single splay fracture, formed under tension, propagating from each end of the fault at an
178 angle of 70˚ measured anticlockwise from the plane of the fault. Due to the asymmetry of
179 the fault in the domain, damage progresses more rapidly at the upper fault tip.
180 Simulations (not shown here) with a central fault predict the evolution of symmetric
181 damage zone structures. The results in Figure 1 are in keeping with LEFM, with the final
182 structure being similar to that in Figure 7a of [*Burgmann et al.*, 1994] where tensile wing
183 cracks are predicted (using a steady-state model) to initiate at 70˚ with a boundary
184 condition of a prescribed shear force applied to the pre-existing fault.
185
186 Figure 1 demonstrates that MOPEDZ can predict the evolution of fault zone structures
187 similar to those of other authors. In the following sections, we use the novel aspects of

188 MOPEDZ to explore *temporal* damage zone evolution under differing conceptual
189 scenarios. We investigate for the first time, the effects on temporal and spatial damage
190 zone evolution of: progressive breakdown of the rock; the magnitude and orientation of
191 the confining stress; the host rock heterogeneity.
192
193 *How Does Damage to Rocks Progressively Occur?*
194 The method by which the material properties of a finite element should be changed as it
195 becomes progressively more fractured is dependent on the how the process of fracturing
196 is conceptualized i.e. the micro-scale processes that represent different bulk weakening
197 behaviors. There are two possible scenarios for the failure process within the elements.
198 The first scenario is that upon failure, a single fracture occurs that spans the whole
199 element, and subsequent failure produces either further smaller fractures that propagate
200 off this fracture or increases the aperture on the original fracture, resulting in progressive
201 weakening of the element (Figure 2a). The second scenario is that when the confining
202 stress is sufficiently high, many locations fail within the element, producing a large
203 number of microfractures. Further stress increases cause the microfractures to eventually
204 coalesce and a single main fracture dominates and spans the whole of the element (Figure
205 2b). Scenario 1 is equivalent to a large drop in strength followed by progressive
206 continued strength breakdown (infilling with weak minerals [*Niemeijer and Spiers*, 2005]
207 or absorption of water into fault gouge [*Morrow et al.*, 2000]). Scenario 2 would
208 correspond to progressive strength breakdown followed by a large drop in strength. This
209 would be equivalent to the process zone model for fracture growth [*Lockner et al.*, 1992].
210 Both of these scenarios ultimately result in a similar reduction of bulk material properties

211 for an element that represents both microscopic damage and a through-going fracture
212 (See final frames of Figure 2).
213
214 To reproduce the above scenarios, MOPEDZ simulations were conducted, again using the
215 parameter values in Table 1, but allowing for a progressive reduction in Young's
216 modulus on a failed element. The first scenario above assumes that most damage occurs
217 in the first failure followed by smaller subsequent failures. This can be expressed as a
218 geometric series, relating the value of the material parameter of interest, D_n, after failure,
219 to the previous value of that material parameter, D_{n-1}

220 $$D_n = \left(\frac{M_f}{M_{hr}} \right)^{\frac{1}{m}} D_{n-1} \qquad \text{where } n = 1,2,...,m \tag{2}$$

221 where M_f is a constant representing the lowest possible value of the material parameter
222 for a completely fractured element, M_{hr} is the value of the material parameter
223 representing intact host rock, m is the number of levels of progressive damage, and D_0 is
224 equal to M_{hr}.
225
226 In the second scenario, microfracturing occurs first, followed by macroscopic failure. In
227 this case, the relative reductions in the above series were reversed to produce small initial
228 reductions in material properties followed by progressively larger ones. Results for these
229 two scenarios allowing a total of three progressive failures of a single element (i.e. m=3)
230 are shown in Figure 3(a) and (b). In the case of initial microfracturing followed by
231 macroscopic failure (i.e. the second scenario above) a single tensile fracture evolves at
232 each fault tip (Figure 3a). By contrast, for immediate macroscopic fracturing of an

element, multiple parallel tensile fractures are observed (Figure 3b). The first fracture to evolve is the longest fracture, at the tip, with subsequent fractures evolving progressively toward the centre of the fault. Fracture length decreases linearly toward the centre of the fault.

To investigate the role of mesh refinement on the development and location of the multiple splay fractures predicted in Figure 3(b), a further simulation was conducted using a finer mesh. Figure 3(c) shows results from a simulation identical to that in Figure 3(b) but with a 160 × 160 mesh i.e. four times the number of elements (this was the limit of the virtual memory available within MATLAB). The preexisting fault for the finer mesh has the same physical thickness as that in the 80×80 case, although its diagonal representation within the square mesh results in a smoother pixelisation of the fault surface. A comparison of Figures 3(b) and (c) shows the results to very similar, both simulations produce parallel splay fractures that decrease in length toward the centre of the fault. In Figure 3c, the finer mesh allows these splays to appear slightly earlier in the simulation and to be closer together, hence they are more concentrated toward the fault tip. Further simulations not shown here, using an even finer adaptive triangular mesh to represent a completely smooth initial fault surface, with an increased length to width ratio (a thinner fault), also produced results similar to those in Figure 3(c): the cracks concentrate at the fault tip and are slightly shorter relative to the length of the original fault. In summary, Figures 3(b) and (c) show that the basic geometry of the results remains very similar as the mesh is refined but that the multiple splays are closer together

255 and more concentrated at the fault tip, this is consistent with observations of multiple
256 splay fractures in the field (see discussion and Figure 8a).
257
258 In all subsequent simulations within this paper, the first scenario of immediate
259 macroscopic fracturing, followed by progressive but decreasing weakening, is adopted to
260 investigate the evolution of *multiple* splay fractures in fault damage zones. This allows
261 for investigation of differing mechanical phenomena to those presented by previous
262 authors such as [*Du and Aydin*, 1995; *Shen and Stephansson*, 1993]. For computational
263 feasibility, the mesh resolution in the following sections is 80×80 which enabled multiple
264 simulations to be performed within a reasonable time scale.
265
266 *How are Fault Damage Zone Structures Influenced by the Confining Stress?*
267 To investigate the role of confining stress in influencing the damage surrounding faults,
268 four different cases were investigated. The final structures obtained for each of these
269 cases are presented in Figure 4. In Figure 4(a) $\sigma_3 = 0$. Figure 4(b) shows results for the
270 same simulation but with $\sigma_1/\sigma_3 = 5$. In this simulation multiple parallel tension cracks are
271 again produced, but here the longest splay fracture is not now associated with the fault
272 tip. In Figure 4(c), the final damage zone structure is shown for $\sigma_1/\sigma_3 = 2.5$. Now a
273 different pattern of damage is observed: wing cracks evolve due to shear failure at the
274 fault tips and propagate at a much lower angle to the original fault plane. In addition to
275 these shear cracks, small tensional cracks form at a higher orientation to the fault and
276 away from the fault tip. In the final simulation (Figure 4d) the boundaries are completely
277 rigid. Here, low angle shear fractures form at the fault tips, and subsequent small

278 perpendicular tertiary fractures then propagate from these shear fractures. The same
279 structures as those in Figure 4(d) were produced as σ_1/σ_3 tended to a value of one (i.e.
280 $\sigma_1 \rightarrow \sigma_3$). The results in Figure 4 imply that for large differential stress (i.e. $\sigma_1 \gg \sigma_3$)
281 multiple parallel tension fractures are formed, whereas for small differential stress (σ_1
282 close to σ_3) single shear fractures form at the fault tip followed by small higher angle
283 tension fractures.
284
285 The effect of varying the orientation of the maximum principal stress with respect to the
286 pre-existing fault is examined in Figure 5. Simulations were conducted for faults at
287 angles of 30˚, 45˚, 60˚ and 75˚ to σ_1 for the two extreme cases in Figure 4 of $\sigma_3 = 0$ and of
288 rigid lateral boundaries, from here termed high and low differential stress respectively.
289 For high differential stress (Figure 5a) all wing cracks form in tension and ultimately
290 propagate in the direction of the maximum principal stress. Figure 5a shows that faults at
291 low angles to the maximum principal stress (30˚ and 45˚) produce single curved splay
292 fractures. As the angle between the fault and σ_1 increases, multiple parallel fractures
293 evolve that decrease in length toward the centre of the fault. Once the fault is oriented at
294 75˚ to σ_1 the geometry of the fracturing becomes more erratic, splay fractures evolve on
295 both sides of the fault at the same tip, and there is no clear pattern to fracture length. In
296 the case of low differential stress (Figure 5b) the predicted damage zone structures are
297 very different. For a fault at an angle of 30˚ to σ_1, wing cracks form in shear and
298 propagate back into the compressive quadrant. As the angle increases, shear fractures
299 begin to propagate at the fault tip at an angle of around 35˚ to the original fault. For large

300 angles, short tension fractures also form away from the fault tip at an angle of 85˚ to the
301 original fault.
302
303 *Does Host Rock Heterogeneity Affect Damage Zone Formation?*
304 To explore the effect of host rock heterogeneity, simulations were conducted using both
305 purely random and spatially correlated fields for host rock material properties. Six
306 realizations were simulated for each statistical material property distribution, in
307 conditions of high differential stress. Final damage zone structures for two of the
308 realizations of the host rock material properties in each case are shown in Figure 6.
309 Figure 6 (row 1) shows final damage zone structures for an uncorrelated, purely random
310 field where the mean Young's modulus of the host rock is 60 GPa (as on previous
311 simulations) with a standard deviation of 1 GPa (i.e. 95% of the field lies between 58GPa
312 and 62 GPa). For comparison, a completely fractured element is represented by a
313 Young's modulus of 1.2 GPa, so the original fault remains quite distinct from any
314 underlying variations in the host rock. Visual inspection of the simulations in Figure 6
315 row 1 shows that both realizations produce multiple parallel splay fractures, but in the
316 first realization a splay fracture forms beyond the fault tip.
317
318 Figure 6, rows 2 to 4, show the results of simulations identical to those in row 1 but with
319 a host rock Young's modulus that is described by a spatially correlated random field. The
320 covariance structure of this field is described by an exponential function of the form
321 $$C(h) = \sigma^2 - \exp(-h/\lambda) \quad (4)$$

where λ is the termed the correlation length and effectively governs the size of the 'patches' of high or low Young's modulus in the host rock, σ^2 is the variance and h is the distance between pairs of points in the field. The results for the final damage zone structure for 3 different correlation lengths are shown in Figure 6 (rows 2 to 4) two realizations are shown for each different correlation length. Again, multiple parallel splay fractures are produced with some of these forming beyond the fault tip. Realizations with high numbers of parallel fractures correspond to those with patches of low host rock Young's modulus adjacent to the fault. For the simulation with the largest correlation length, a shear fracture can be seen propagating from the left hand fault tip. It is clear that whilst the macroscopic damage zone pattern remains very similar in these simulations, the exact locations and frequencies of evolving splay fractures are heavily influenced by the heterogeneous material properties of the host rock.

Discussion

The simulation results presented here have investigated the formation of fractures around a single pre-existing feature (described here as a fault, but which could represent other pre-existing features such as joints and dikes [*d'Alessio and Martel*, 2005]). We have investigated varying the effect of: the conceptual scenario of progressive fracture damage; the orientation of the initial fault with respect to the maximum principal compressive stress; the confining boundary conditions; and the heterogeneity of the host rock material properties. The range of resulting damage zone structural styles are summarized in Figure 7. Typical structures are a) single tensile wing cracks, b) multiple tensile wing cracks, c) unconnected tensile fractures, d) low angle wing cracks that have formed in shear e) low angle shear cracks with tertiary fractures subsequently propagating off their sides, and f) high angle shear fractures that propagate at angles between 180º and 270º (measured anticlockwise from the original fault plane). Interestingly, one key form of damage zone evolution that is not predicted here is an extension of the initial fault in its own plane. Fault plane extension has been previously simulated by [*Du and Aydin*, 1993; 1995], however, in their conceptual model of mechanical failure, tensile failure is suppressed.

Comparison with previous theory and outcrop measurements.

This research has produced tensile wing cracks that vary in angle from 30º to 90º and synthetic shear wing cracks that vary from 23º to 40º. This range is far broader than the range predicted by Linear Elastic Fracture Mechanics [*Pollard and Segall*, 1987] which predicts all fractures should initially propagate at 70º.

358

359 Wing crack measurements on outcrops are generally low, but can range from 15º to 70º.
360 The angles produced by MOPEDZ compare well with field observation of wing crack
361 angles (Table 2). In our simulations, the most influential factor is the orientation of the
362 fault relative to the maximum principal stress direction. Since faults in crystalline rocks
363 are generally thought to evolve from the linking of pre-existing joints [*Martel*, 1990] or
364 dikes [*d'Alessio and Martel*, 2004], the maximum principal stress direction must have
365 originally been aligned with their pre-existing structures. It seems reasonable to presume
366 that smaller rotations of the stress field will be more common than larger ones, and this
367 would result in wing cracks frequently occurring at angles at the lower end of the possible
368 range.

369

370 For a comparison of MOPEDZ with field observations, Figure 8a shows a 14m long fault
371 developed in granodiorite in the Kip Camp area of the Sierra Nevada, California mapped
372 by [*Lim*, 1998]. The length of the wing cracks in Figure 8a is related to distance from the
373 fault tip, with a general decrease in length of the wing cracks as the distance from the
374 fault tip increases. The adjacent MOPEDZ simulation shown compares well with the type
375 of damage shown in [*Lim*, 1998]. The simulation has high differential stress (i.e. $\sigma_1 \gg \sigma_3$)
376 assumes immediate macroscopic damage of the host rock on initial failure, and has a fault
377 inclined at 60º to the maximum principal compressive stress. The simulation produces
378 wing cracks that propagate at around 60º, that are distributed along the length of the joint
379 and that decrease in length as the distance from the tip increases. This simulation suggests
380 that there was high differential stress when fracturing around the fault developed and that

381 the direction of the maximum principal stress for the fault in Figure 8a was
382 approximately north-south.
383
384 Figure 8b shows the Alligerville fault, New York state, mapped by *Vermilye & Scholz*
385 [1998]. The 40m long vertical fault is in quartzite [*Vermilye & Scholz* 1998]. The fault
386 has shear wing cracks that propagate in the compressional quadrants at angles of around
387 225º, which are distributed along the length of the fault, and decrease in length as the
388 distance from the fault tip increases. The fault also shows pressure solution cleavage in
389 the compressional quadrant, striking at approximately -60º. The adjacent MOPEDZ
390 simulation shown in Figure 8b compares well with the Alligerville fault trace. This
391 simulation has confined boundary conditions, assumes immediate macroscopic damage
392 of the host rock on initial failure (Figure 3a) and has an initial fault orientation of 30º to
393 the maximum principal compressive stress. The simulation produces shear wing cracks
394 that propagate from the fault tips into the compressional quadrant at around 242º . In the
395 Alligerville fault, multiple fractures are formed which are not reproduced in the
396 MOPEDZ simulations, this may be due to the heterogeneity of the host rock, or due to the
397 clear deviations from a planar fault surface (which would concentrate stress) that are
398 apparent on the Alligerville fault. Based on our simulations, we suggest that the direction
399 of the maximum principal stress around the Alligerville fault was approximately north-
400 west/south-east when fracturing developed, and that the differential stress was low.
401
402

Implications for the temporal sequence of multiple wing cracks.

A number of conceptual temporal sequences for the evolution of multiple splay fractures have been proposed e.g. [*Martel and Pollard*, 1989]. Four conceptual temporal sequences (S1 to S4) are possible (Figure 9). In S1, wing cracks form behind (i.e. away from) the fault tip, and then further wing cracks form progressively nearer to the fault tip (Figure 9a); this is essentially the sequence proposed in [*Martel and Pollard*, 1989] and simulated for seismic rupture in [*Dalguer et al.*, 2003]. In S2, wing cracks form initially at the tips of the fault and then further wing cracks form at locations that are progressively closer to the middle of the joint (Figure 9b). In S3, wing cracks form at the tips, subsequently the fault extends in its original plane, and then further wing cracks form at the new tips (Figure 9c). Finally in S4, wing cracks form at the tips of the fault, parallel wing cracks form that are away from and unconnected to the fault tip, the tip then extends and connects to these parallel cracks (Figure 9d) .

Based on the simulations presented here, the most likely sequence for temporal evolution is that of S2 (Figure 9b). Almost all MOPEDZ simulations predict the first wing crack to occur at the fault tip. In general, further wing cracks then form progressively further away from the tip toward the centre of the fault. This temporal sequence matches that of S2 in Figure 9b. However, in simulations with low differential stress and an angle of at least 75˚ to the maximum principal compressive stress the first wing cracks are predicted to initiate away from the fault tip (S1, Figure 9a). For these high angle faults, the formation of wing cracks is predicted to be highly irregular in length, with a few cracks also appearing in the compressional quadrant.

425 Finally, in a few of the realizations incorporating a fault within a heterogeneous host
426 rock, fractures occur beyond the tip of the fault without any extension of the original fault
427 in its own plane. Once these fractures have formed it is possible that subsequent
428 fracturing could link these off-tip fractures (sequence S4, Figure 9d) but this final linking
429 stage has not been produced here.
430
431 *Implications for fluid flow*
432 The future application of physically-based simulation models to improve estimates of
433 fault hydraulic properties in the subsurface, depends critically on being able to accurately
434 predict the orientation, frequency and connected nature of evolving fractures in the
435 damage zone. In this paper, we demonstrate that it is possible to simulate the spatial and
436 temporal evolution of multiple splay fractures from a single pre-existing fault.
437 Simulations are compared with field observation data and the orientation of the predicted
438 fractures compares well with observed fault zone geometries. The model can now
439 confidently be applied to investigate more complex fault zone geometries, such as fault
440 zone development from linkage of pre-existing joints [*Martel*, 1990], and combined with
441 fluid flow simulation [*Willson et al.*, 2005] for bulk permeability estimation.
442
443 **Conclusions**
444 We present a new model, MOPEDZ, for dynamic simulation of multiple and single splay
445 fractures originating from a single feature such as a fault, joint or dike. The model is
446 based on a finite element solution of Navier's equation using a combined Mohr-Coulomb
447 and tensile failure criterion. Simulations compare well with field observations of fault

zone geometry. Investigations of damage zone evolution under differing boundary conditions and material properties predict that:

- Changing the conceptual sequence of microscopic versus macroscopic fracturing of an element results in important differences in the structure of the damage zone around slipping faults. Simulations show that a conceptual sequence of microscopic damage followed by macroscopic failure tends to produce single splay fractures at the fault tip, whereas immediate macroscopic failure produces multiple parallel splay fractures that decrease in length away from the fault tip.
- Due to the combined Mohr Coulomb and tensile failure criteria, which allows both shear and tensile failure, the orientations of damage zone features surrounding the fault are heavily influenced by the differential stress. For low differential stress, simulations predict single shear fractures at the fault tip that propagate at a low angle to the fault. For high differential stress,, fractures form in tension at the fault tips followed by multiple parallel fractures that are progressively closer to the fault centre and shorter in length.
- Faults that are reactivated at a high angle to the maximum principal compressive stress form multiple parallel splay fractures. By comparison, faults at a low angle to the maximum principal stress, form single fractures at the fault tips. For simulations where the differential stress is low, these single fractures propagate into the compressional quadrant.
- Host rock heterogeneity effects the locations of evolving splay fractures sometimes causing them to originate beyond the tip of the original fault.

- In the case of multiple splay fractures, simulations generally support a temporal evolution in which the initial fracture occurs at the fault tip. This is then followed by the evolution of other parallel features that are progressively both shorter in length and further from the tip.

Acknowledgements

This research was funded by the Engineering and Physical Sciences Research Council, UK grant number GR/R69464/01, and the authors would like to thank them for their support. Heather Moir ran the model for later versions of the figures. We thank Jonathan Caine and two anonymous reviewers for constructive comments.

References List

Anderson, R. N., P. Flemings, S. Losh, J. Austin, and R. Woodhams (1994), Gulf-of-Mexico Growth Fault Drilled, Seen as Oil, Gas Migration Pathway, *Oil & Gas Journal*, *92*(23), 97-104.

Aydin, A. (2000), Fractures, faults and hydrocarbon entrapment migration and flow, *Marine and Petroleum Geology*, *17*, 797-814.

Burgmann, R., D. D. Pollard, and S. J. Martel (1994), Slip distributions on faults: effects of stress gradients, inelastic deformation, heterogeneous host-rock stiffness, and fault interaction, *Journal of Structural Geology*, *16*(12), 1675-1690.

Byerlee, J. D. (1967), Frictional characteristics of granite under high confining pressure., *Journal of Geophysical Research*, *72*, 3639-3648.

Caine, J. S., J. P. Evans, and C. B. Forster (1996), Fault zone architecture and permeability structure, *Geology*, *24*(11), 1025-1028.

COMSOL (2004), FEMLAB, edited, COMSOL AB.

Cruikshank, K. M., G. Zhao, and A. M. Johnson (1991), Analysis of minor fractures associated with joints and faulted joints, *Journal of Structural Geology*, *13*(8), 865-886.

d'Alessio, M. A., and S. J. Martel (2004), Fault terminations and barriers to fault growth, *Journal of Structural Geology*, *26*, 1885-1896.

d'Alessio, M. A., and S. J. Martel (2005), Development of strike-slip faults from dikes, Sequoia National Park, California, *Journal of structural geology*, *27*(1), 35-49.

Dalguer, L. A., K. Irikura, and J. D. Riera (2003), Simulation of tensile crack generation by three-dimensional dynamic shear rupture propagation during an earthquake, *J. Geophys. Res.-Solid Earth*, *108*(B3).

do Nascimento, A. F., R. J. Lunn, and P. A. Cowie (2005), Modeling the heterogeneous hydraulic properties of faults using constraints from reservoir-induced seismicity, *J. Geophys. Res.-Solid Earth*, *110*(B9).

Du, Y. J., and A. Aydin (1993), The Maximum Distortional Strain-Energy Density Criterion for Shear Fracture Propagation with Applications to the Growth Paths of En-Echelon Faults, *Geophysical Research Letters*, *20*(11), 1091-1094.

Du, Y. J., and A. Aydin (1995), Shear Fracture Patterns and Connectivity at Geometric Complexities Along Strike-Slip Faults, *J. Geophys. Res.-Solid Earth*, *100*(B9), 18093-18102.

Evans, K. F. (2005), Permeability creation and damage due to massive fluid injections into granite at 3.5 km at Soultz: 2. Critical stress and fracture strength, *J. Geophys. Res.-Solid Earth*, *110*(B4).

Evans, K. F., A. Genter, and J. Sausse (2005a), Permeability creation and damage due to massive fluid injections into granite at 3.5 km at Soultz: 1. Borehole observations, *Journal of Geophysical Research*, *110*(B04203).

Evans, K. F., A. Genter, and J. Sausse (2005b), Permeability creation and damage due to massive fluid injections into granite at 3.5 km at Soultz: 1. Borehole observations, *J. Geophys. Res.-Solid Earth*, *110*(B4).

Evans, K. F., H. Moriya, H. Niitsuma, R. H. Jones, W. S. Phillips, A. Genter, J. Sausse, R. Jung, and R. Baria (2005c), Microseismicity and permeability enhancement of hydrogeologic structures during massive fluid injections into granite at 3 km depth at the Soultz HDR site, *Geophysical Journal International*, *160*(1), 388-412.

Fairley, J. P., and J. J. Hinds (2004), Rapid transport pathways for geothermal fluids in an active Great Basin fault zone, *Geology*, *32*(9), 825-828.
Galli, G., A. Grimaldi, and A. Leonardi (2004), Three-dimensional modelling of tunnel excavation and lining, *Computers and Geotechnics*, *31*(3), 171-183.
Lim (1998), Small strike slip faults in granitic rock: implications for three-dimensional models, Masters Thesis thesis, Utah State University, Logan, Utah.
Lockner, D. A., J. D. Byerlee, V. Kuksenko, A. Ponomarev, and A. Sidorin (1992), Observations of quasistatic fault growth from acoustic emissions, in *Fault mechanics and transport properties of rocks*, edited by B. Evans and T.-F. Wong, pp. 1-31, Academic Press, San Francisco.
Losh, S. (1998), Oil Migration in a Major Growth Fault: Structural Analysis of the Pathfinder Core, South Eugene Island Block 330 Field, Offshore Louisiana, *AAPG Bulletin*, *82*(9), 1694-1710.
Losh, S. (2006), Episodic fluid flow and aseismic slip, *AGU Monograph*.
Martel, S. J., and D. D. Pollard (1989), Mechanics of Slip and Fracture Along Small Faults and Simple Strike-Slip-Fault Zones in Granitic Rock, *Journal of Geophysical Research-Solid Earth and Planets*, *94*(B7), 9417-9428.
Martel, S. J. (1990), Formation of Compound Strike-Slip-Fault Zones, Mount Abbot Quadrangle, California, *Journal of Structural Geology*, *12*(7), 869-&.
Martin, C. D. (1997), Seventeenth Canadian geotechnical colloquium: the effect of cohesion loss and stress path on brittle rock strength, *Can Geotech Journal*, *34*(5), 698-725.
Morrow, C. A., D. E. Moore, and D. A. Lockner (2000), The effect of mineral bond strength and adsorbed water on fault gouge frictional strength, *Geophysical Research Letters*, *27*(6), 815-818.
Niemeijer, A. R., and C. J. Spiers (2005), Influence of phyllosilicates on fault strength in the brittle-ductile transition: Insights from rock analogue experiments, paper presented at High-strain zones: Structure and physical properties, Geological Society of London Special Publications.
Pollard, D. D., and P. Segall (1987), Theoretical displacements and stresses near fractures in rock: with applications to faults, joints, veins, dykes and solution surfaces, in *Fractals in the Earth Sciences*, edited by A. B, pp. 89-105, Plenum Press New York.
Segall, P., and D. D. Pollard (1983), Nucleation and Growth of Strike Slip Faults in Granite, *Journal of Geophysical Research*, *88*(NB1), 555-568.
Shen, B., and O. Stephansson (1993), Numerical-Analysis of Mixed Mode-I and Mode-Ii Fracture Propagation, *Int. J. Rock Mech. Min. Sci.*, *30*(7), 861-867.
Tang, C. A. (1997), Numerical Simulation of Progressive Rock Failure and Associated Seismicity, *International Journal of Rock Mechanics and Mining Sciences*, *34*(2), 249-261.
Turcotte, D., and J. Schubert (1982), *Geodynamics*, 2nd Edition ed., Cambridge University Press, Cambridge.
Vermilye, J. M., and C. H. Scholz (1998), The process zone: A microstructural view of fault growth, *J. Geophys. Res.-Solid Earth*, *103*(B6), 12223-12237.
Wibberley, C. A. J., and T. Shimamoto (2003), Internal structure and permeability of major strike-slip fault zones: the Median Tectonic Line in Mie Prefecture, Southwest Japan, *Journal of Structural Geology*, *25*(1), 59-78.

Willson, J. P., R. J. Lunn, Z. K. Shipton, and P. A. Cowie (2005), Modelling hydraulic permeability evolution in fault damage zones, paper presented at EUROCK 05, A.T. Balkema & G. Westers, Brno.
Yamashita, T. (2000), Generation of microcracks by dynamic shear rupture and its effects on rupture growth and elastic wave radiation, *Geophysical Journal International*, *143*(2), 395-406.

Figure 1 Temporal development of wing cracks at the tips of a single fault, using the parameters listed in Table 1 and σ_3=0. The maximum principal stress (σ_1) is oriented top to bottom in these simulations. Each frame shows the structure that has developed by increasing the boundary displacement, Δy, to the amount indicated. The grey scale represents material Young's modulus; grey is unfractured (60GPa) and black is fractured (1.2GPa). The angle between the fault and the wing crack is measured anticlockwise from the plane of the fault

Figure 2 Sequences of progressive fracturing for a single finite element **a)** development of fracturing assumes that the major fracture happens first, and subsequent fractures are smaller (shown for three steps), **b)** development of fracturing assumes that microfractures occur first, and larger fractures develop through coalescence of these fractures.

Figure 3 Temporal damage zone progression **a)** assuming initial macroscopic failure with an 80×80 mesh (see Figure 2a) **b)** initial microscopic failure with an 80×80 mesh (see Figure 2b) **c)** assuming initial macroscopic failure with an 160×160 mesh (see Figure 2a) **d)** assuming initial microscopic failure with an 160×160 mesh (see Figure 2b). The maximum principal stress (σ_1) is oriented top to bottom.

Figure 4 Comparison of simulations with different ratios of σ_1 to σ_3. The maximum principal stress (σ_1) is oriented top to bottom. **a**) $\sigma_3 = 0$ (this is a reproduction of the final damage structure in Figure 3a), **b)** a ratio of $\sigma_1 / \sigma_3 = 5$, **c)** a ratio of $\sigma_1 / \sigma_3 = 2.5$, **d)** rigid left and right boundaries.

Figure 5 Resulting structures when varying fault orientation for a boundary displacement of approximately 6.8mm. The orientation between the fault and σ_1 (oriented top to bottom) is 30º, 45º, 60º and 75º for **a)** high differential stress and **b)** low differential stress.

Figure 6 Resulting structures using a heterogeneous Young's modulus field for a boundary displacement of approximately 3mm. Each simulation starts with a different heterogeneous Young's modulus matrix. The maximum principal stress (σ_1) is oriented top to bottom. There are 2 realisations each of a purely random field and of three different of correlation lengths of 0.15m, 0.375m and 0.45m. Colour scale is logarithmic and indicates Young's modulus.

Figure 7 Six fault tip structural styles that have been produced with MOPEDZ.

Figure 8 a) A fault in granodiorite showing multiple wing cracks distributed along its entire length [*Lim*, 1998] alongside a structure produced by MOPEDZ with high differential stress starting with a fault inclined at 60º to the maximum principal stress. The mapped fault strikes at 57º and dips 81º to the south, the grey rectangle on the map indicates ground cover, and it is presumed the fault is continuous [*Lim*, 1998]. **b)** Outcrop map of a fault after Vermilye & Scholz [1998] alongside a simulation produced by MOPEDZ with low differential stress, starting from a fault that is inclined at 30º to the maximum principal compressive stress

Figure 9 Four possible sequences for the formation of multiple wing cracks. a) cracks form behind the fault tip and further fractures occur towards the tip, b) cracks form at the fault tip and further fractures occur towards the centre, c) cracks always form at the tip, but the fault extends in length, d) cracks form at the tip, further fractures form beyond the fault tip which are subsequently linked by extension of the fault

Domain length	3m	
Domain width	3m	
Matrix rows	80	
Matrix columns	80	
Fracture length	1.6875m	
Fracture rotation	60º	
Host rock Young's Modulus	60 GPa	[*Martin*, 1997] [*Turcotte and Schubert*, 1982]
Host rock Poisson's ratio	0.2	[*Turcotte and Schubert*, 1982]
Young's Modulus of fractured element	1.2 GPa	[*Segall and Pollard*, 1983]
Poisson's ratio of fractured element	0.02	
C_0 (Shear strength)	130 MPa	[*Martin*, 1997]
μ (Coefficient of friction)	0.6	[*Byerlee*, 1967]
T_0 (Tensile strength)	10 MPa	[*Martin*, 1997]
Failed locations Limit	10	
Young's modulus of the platen	120 GPa	

Table 1 MOPEDZ simulation parameters, where relevant the right hand column contains the reference from which the value of the mechanical property for granite was derived

Author	Range of wing crack angles	Rock type and location
[*Lim*, 1998]	20º to 70º	Granite, Sierra Nevada, California
[*Segall and Pollard*, 1983]	15º to 35º	Granite, Sierra Nevada, California
[*Cruikshank et al.*, 1991]	35º to 50º	Sandstone, Arches National Park, Utah

Table 2 Wing crack angles measured in the field

i) Δy = 0

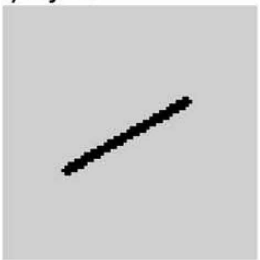

ii) Δy = 0.0002

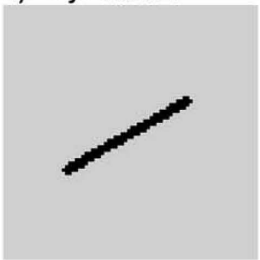

iii) Δy = 0.0006

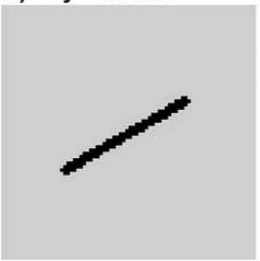

iv) Δy = 0.0008

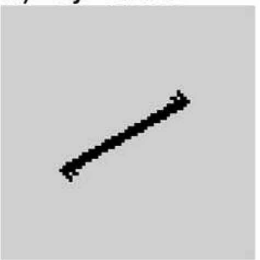

v) Δy = 0.001

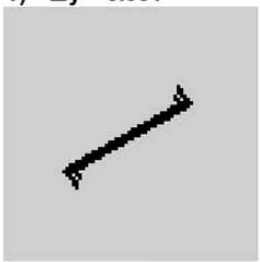

vi) Δy = 0.0012

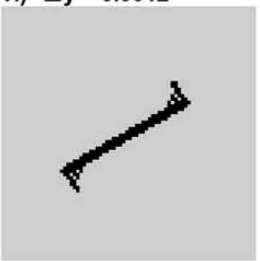

vii) Δy = 0.0014

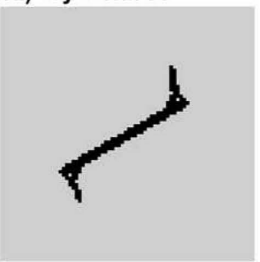

viii) Δy = 0.0016

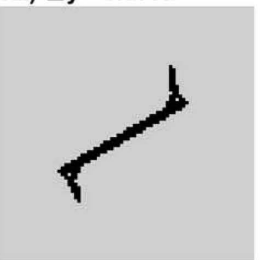

ix) Δy = 0.0018

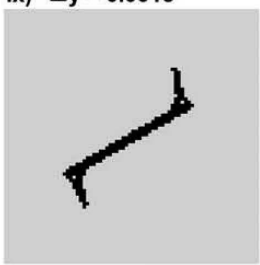

x) Δy = 0.002

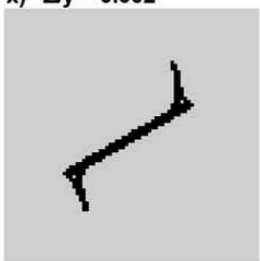

xi) Δy = 0.0022

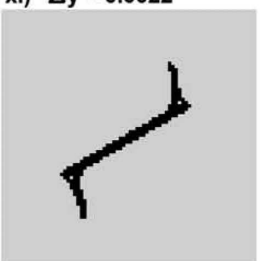

xii) Δy = 0.0024

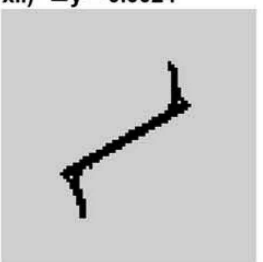

xiii) Δy = 0.0026

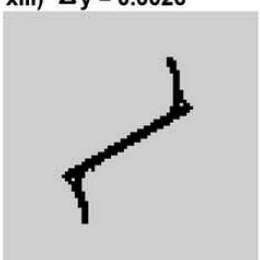

xiv) Δy = 0.0028

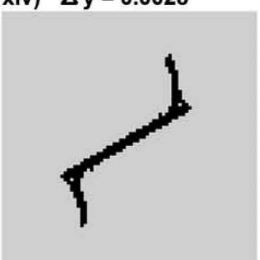

xv) Δy = 0.0029

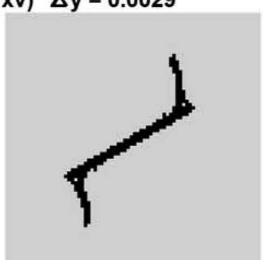

xvi) Δy = 0.00295

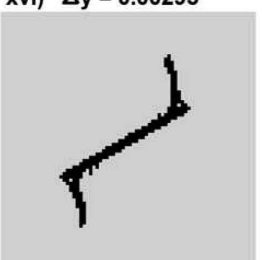

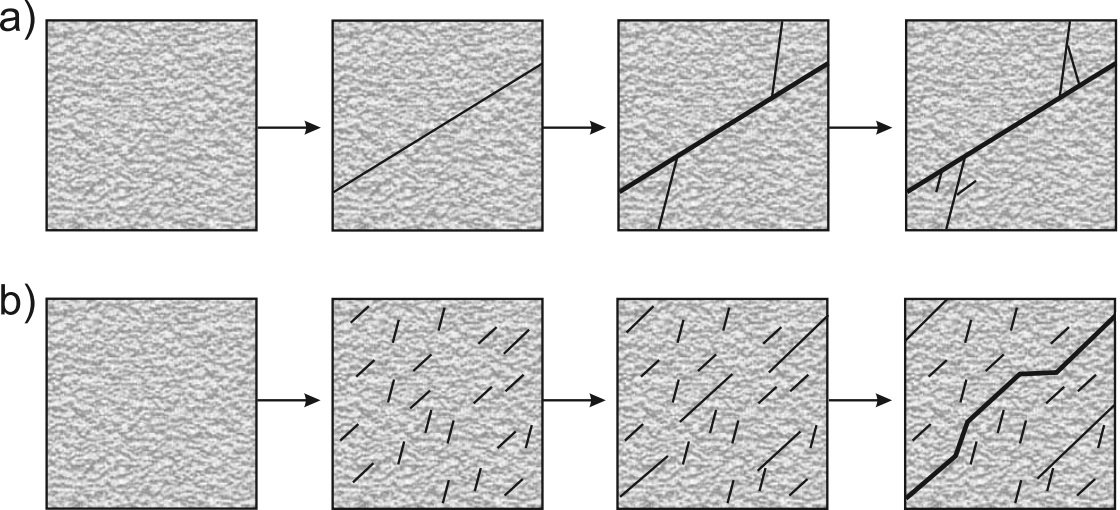
a)
b)

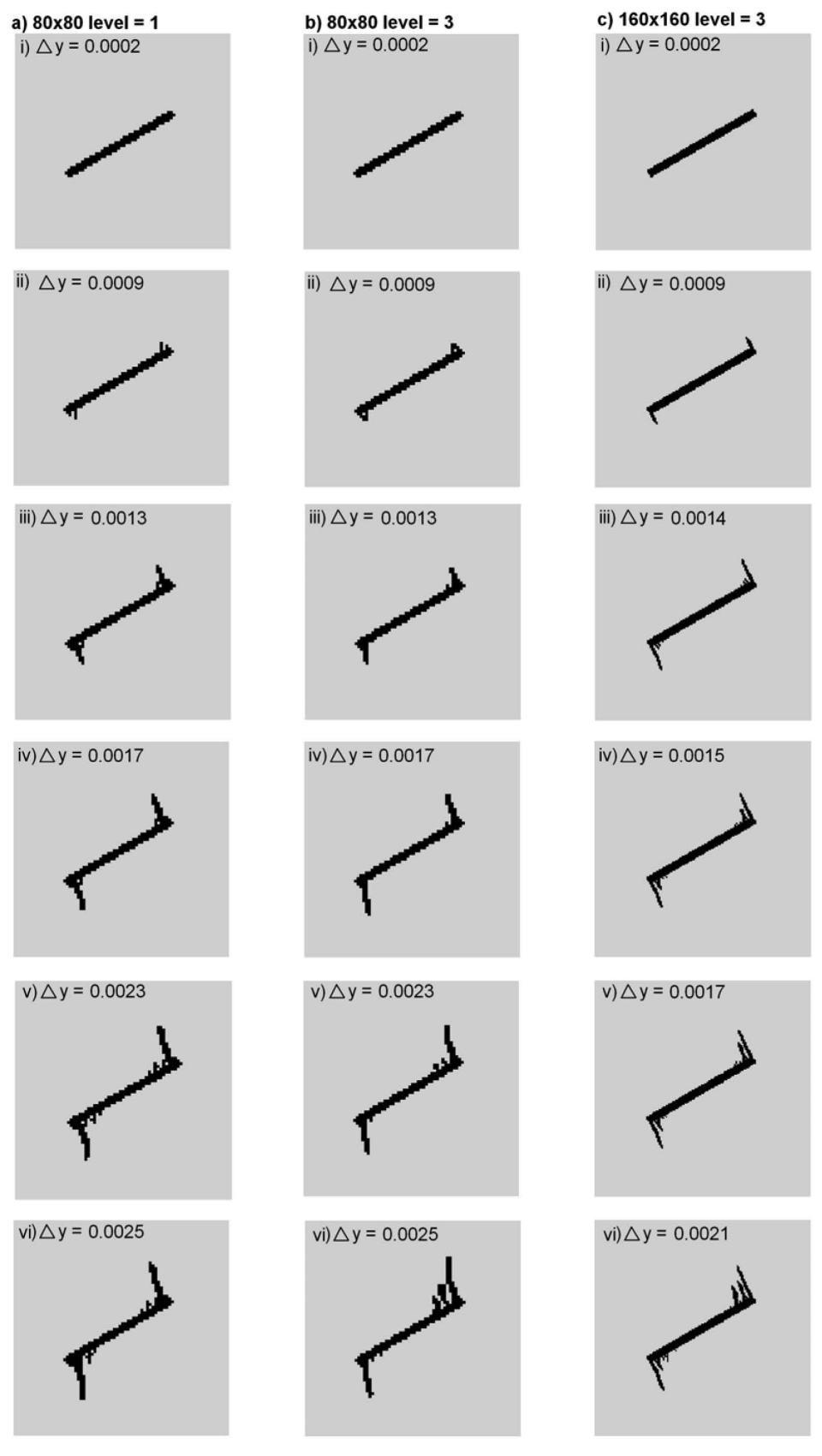
a) 80x80 level = 1
b) 80x80 level = 3
c) 160x160 level = 3
i) △y = 0.0002
i) △y = 0.0002
i) △y = 0.0002
ii) △y = 0.0009
ii) △y = 0.0009
ii) △y = 0.0009
iii) △y = 0.0013
iii) △y = 0.0013
iii) △y = 0.0014
iv) △y = 0.0017
iv) △y = 0.0017
iv) △y = 0.0015
v) △y = 0.0023
v) △y = 0.0023
v) △y = 0.0017
vi) △y = 0.0025
vi) △y = 0.0025
vi) △y = 0.0021

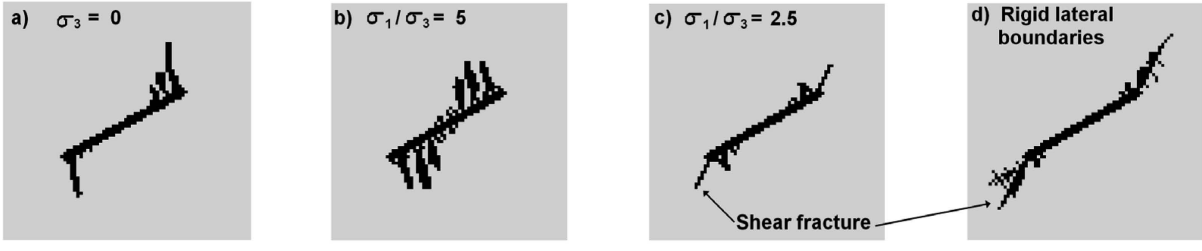
a) $\sigma_3 = 0$
b) $\sigma_1 / \sigma_3 = 5$
c) $\sigma_1 / \sigma_3 = 2.5$
d) Rigid lateral boundaries
Shear fracture

a) High differential stress

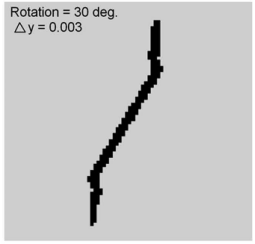

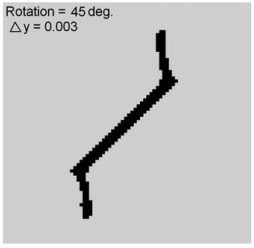

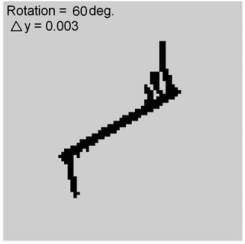

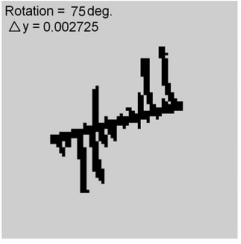

b) Low differential stress

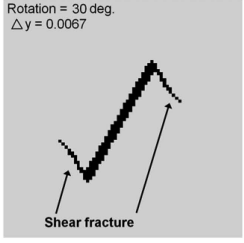

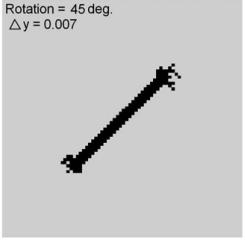

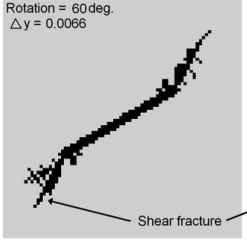

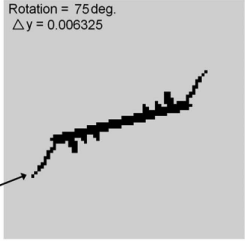

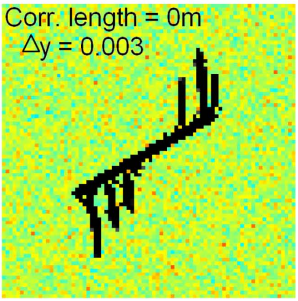
Corr. length = 0m
Δy = 0.003

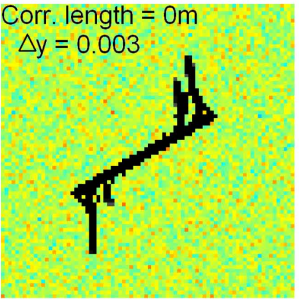
Corr. length = 0m
Δy = 0.003

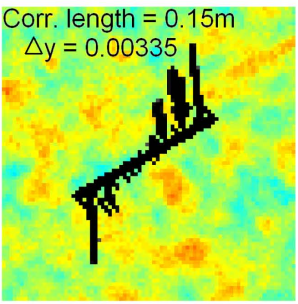
Corr. length = 0.15m
Δy = 0.00335

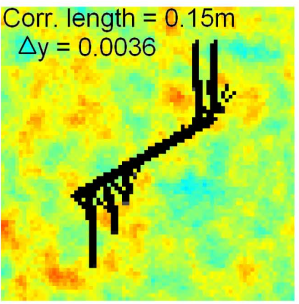
Corr. length = 0.15m
Δy = 0.0036

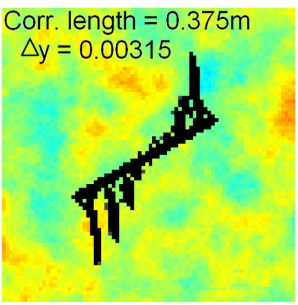
Corr. length = 0.375m
Δy = 0.00315

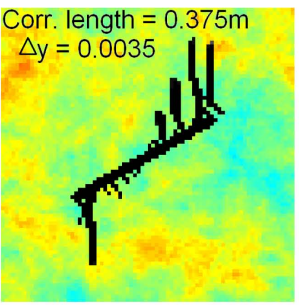
Corr. length = 0.375m
Δy = 0.0035

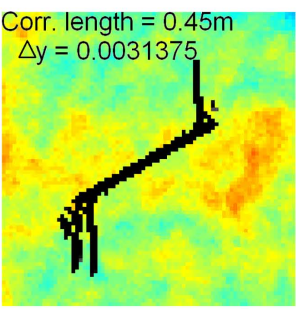
Corr. length = 0.45m
Δy = 0.0031375

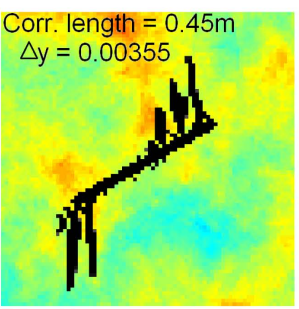
Corr. length = 0.45m
Δy = 0.00355

(1) Single tensile wing cracks

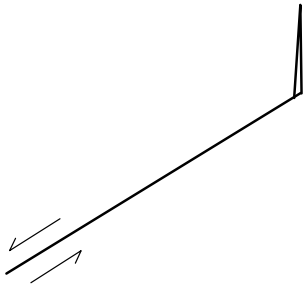

(2) Multiple tensile wing cracks

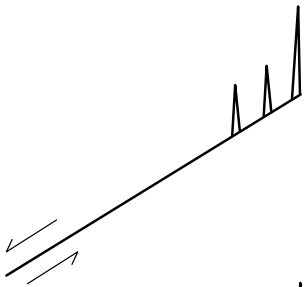

(3) Fractures beyond the joint tip

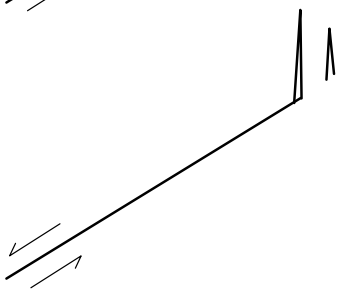

(4) Shear wing cracks

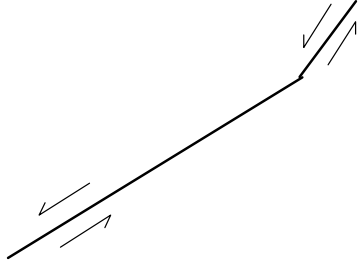

(5) Shear wing cracks with tertiary antithetic fractures

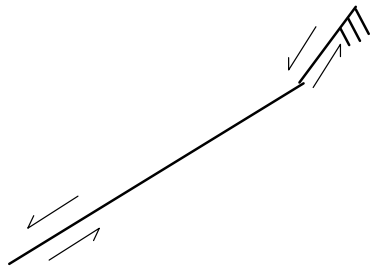

(6) Shear fractures propagating in the compressional quadrant

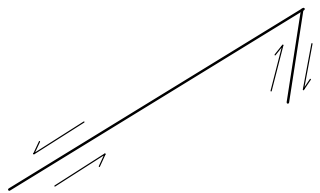

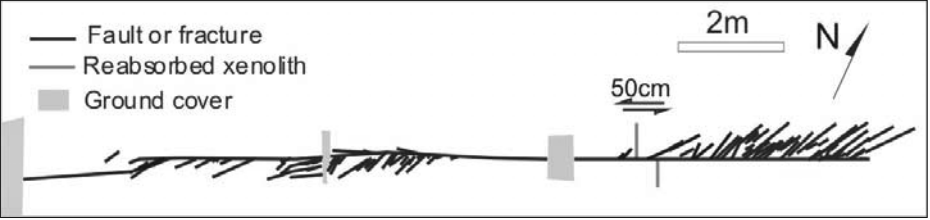
Fault or fracture
Reabsorbed xenolith
Ground cover
2m
N
50cm

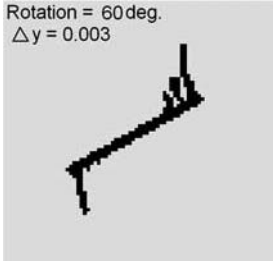
Rotation = 60 deg.
△y = 0.003

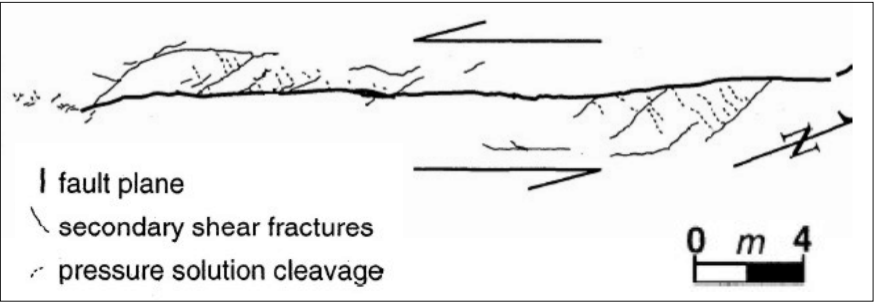
fault plane
secondary shear fractures
pressure solution cleavage
0 m 4

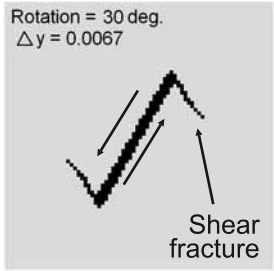
Rotation = 30 deg.
△y = 0.0067
Shear fracture

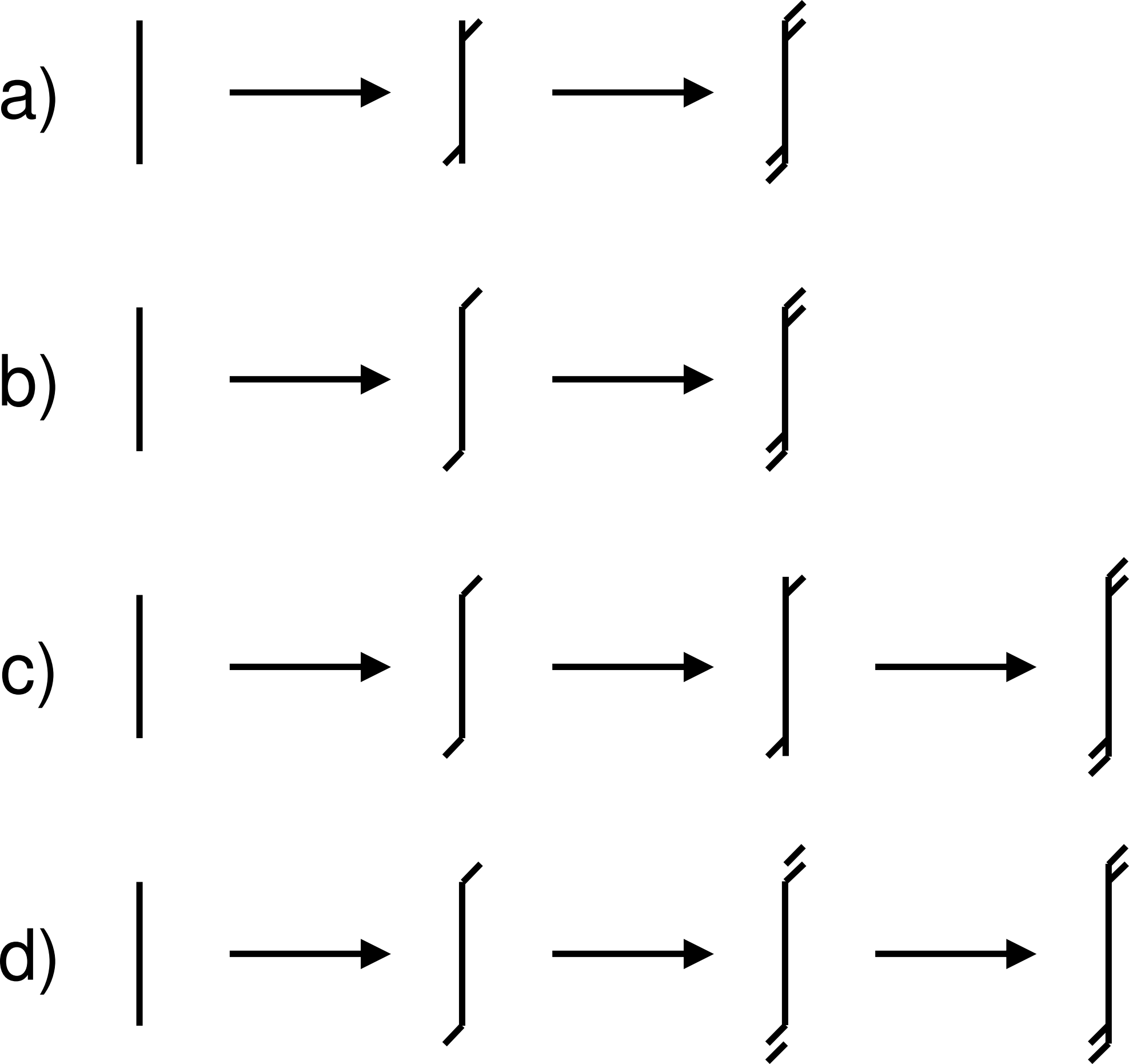
a)
b)
c)
d)